Wei Li (Orcid ID: 0000-0002-2979-5738)

Colombera Luca (Orcid ID: 0000-0001-9116-1800)

Yue Dali (Orcid ID: 0000-0001-8918-9513)

Mountney Nigel P (Orcid ID: 0000-0002-8356-9889)

Controls on the morphology of braided rivers and braid bars: An empirical characterization of numerical models

WEI LI [1,2,3], LUCA COLOMBERA [3,4], DALI YUE [1,2], NIGEL P. MOUNTNEY [3]

1. State Key Laboratory of Petroleum Resources and Prospecting, China University of Petroleum (Beijing), Beijing, 102249, China

2. College of Geosciences, China University of Petroleum (Beijing), Beijing, 102249, China

3. Fluvial, Eolian & Shallow-Marine Research Group, School of Earth & Environment, University of Leeds, Leeds, LS2 9JT, UK

4. Now at: Dipartimento di Scienze della Terra e dell'Ambiente, Università di Pavia, Via Ferrata 1, 27100, Pavia, Italy

Corresponding author: Dali Yue (yuedali@cup.edu.cn)

Email address of other authors: wei_li_geologist@qq.com (Wei Li); luca.colombera@unipv.it (Luca Colombera); n.p.mountney@leeds.ac.uk (Nigel P. Mountney)

Short Title – Controls on the morphology of braided rivers

Associate Editor – Charlie Bristow

ABSTRACT

Braided rivers exhibit highly variable morphologies, morphodynamic behaviours and resulting depositional records. To evaluate relationships between characteristics of braided-river channel belts and river depth, water discharge and streambed gradient, 39 numerical modelling experiments were conducted with the software Delft3D to simulate braided-river evolution under a broad range of boundary conditions. Data from model outputs were integrated with observations from 63 natural braided rivers differing with respect to river depth and streambed gradient. The modelled rivers each underwent similar evolutions, yet each culminated in markedly different final river morphologies, dependent on discharge and riverbed gradient. The rivers underwent evolutionary stages of: (i) formation of transverse unit bars with limited relief from an initially featureless bed; (ii) channel development around bars and in some cases dissecting transverse unit bars; (iii) formation of relatively simpler compound bars; and (iv) amalgamation of these simpler compound bars into more complex compound bars. Quantitative relationships relating to braided-river channel-belt morphology and organization are established, and the following results are noted: (i) bar elongation (length-to-width ratio) is correlated positively with riverbed gradient; (ii) bar height and area are correlated positively with discharge, and negatively with riverbed gradient; (iii) the river depth is the main predictor of mean braid-bar area; (iv) the degree of braiding is primarily associated with river width-to-depth ratio and riverbed gradient. Results arising from this research improve our understanding of controls on the morphology and architectures of braided fluvial channel belts; they provide a novel empirical characterization that can be applied for predicting channel depth, bar morphology, streambed gradient, and degree of braiding of modern fluvial systems and of the formative rivers of ancient preserved successions.

Key words: braided river, Delft3D, discharge, gradient, morphology, numerical simulation

INTRODUCTION

Braided rivers are common landforms of continental environments, and their deposits are important components of the Earth's sedimentary record, both recent and ancient (Bridge & Lunt, 2006; Yao *et al.*, 2018). Understanding the morphology and sedimentary processes of braided rivers has enabled the sedimentary facies architecture of their deposits to be explained in terms of formative river behaviour. Understanding the controls that determine river morphology is important for the prediction of formative depositional conditions and resultant sedimentary architectures in braided fluvial successions (Bridge *et al.*, 1986; Stecca *et al.*, 2019; Limaye, 2020).

There exist multiple potential controls on river morphology, evolution and resulting preserved architectures, which include water discharge, tectonic forcing of longitudinal gradient, sediment flux and riverbed materials (Schumm, 1985; Smith *et al.*, 2006; Holbrook & Schumm, 1999). Notably, observations of natural rivers and flume experiments indicate that the geometry and dynamics of braided rivers vary significantly with both riverbed gradient (Holzweber *et al.*, 2014; Castelltort, 2018) and water discharge (Kleinhans *et al.*, 2014; Sun *et al.*, 2015). However, generalized depositional models relating to braided river morphology that account for externally imposed riverbed gradient and discharge have yet to be established. Thus, there still exists a need to quantify braided-river morphology as a function of discharge and riverbed gradient.

In braided rivers, unit bars are often defined as relatively unmodified bars whose morphologies are mainly determined by relatively uninterrupted depositional processes (Smith, 1974). Unit bars commonly tend to coalesce into compound bars (Bridge & Lunt, 2006; Li *et*

al., 2015; Schuurman & Kleinhans, 2015). Relatively simpler compound bars, produced by the welding of migrating unit bars, can themselves amalgamate to form larger compound bars that record a more complex accretion history (Rice *et al.*, 2009; Nicholas *et al.*, 2013).

A long-established approach to the study of the morphology and sedimentology of braided rivers has been the use of numerical modelling (Murray & Paola, 1994; Bernini *et al.*, 2006). One particular class of numerical modelling that has received notable attention is physics-based modelling, for example as implemented in the software Delft3D (Baar *et al.*, 2019; Crosato & Saleh, 2011). Delft3D is a physics-based morphodynamic model in which the hydrodynamics are based on the Reynolds-averaged Navier-Stokes equations (Caldwell & Edmonds, 2014; Deltares, 2014). Although the dynamics and evolution of braided rivers have long been studied with Delft3D simulations (Schuurman *et al.*, 2013; Schuurman & Kleinhans, 2015), a significant factor has not been considered in depth by earlier research: the relationship between riverbed gradient and braid-bar evolution and morphology has hitherto not been examined in detail; instead, prior modelling has generally employed a single input longitudinal gradient.

The aim of this work is to elucidate how the morphology of braided channel belts and their constitutive landforms (braid bars and channels) vary as a function of water discharge, river depth and riverbed gradient. To achieve this, a series of braided rivers are simulated using Delft3D, and the morphology of bars observed in natural braided channel belts is analysed using remote-sensing data from Google Earth and published data. Specific objectives of this research are as follows: (i) to model the evolution of braided rivers through stages of morphodynamic change that can be recognized in real-world rivers; (ii) to assess and quantify variability in morphological characteristics of braided rivers in relation to differences in discharge, river depth and longitudinal riverbed gradients; and (iii) to propose predictive relationships that can be applied to predict the morphology and bathymetry of modern fluvial

systems, as well as palaeohydrological characteristics of formative braided rivers of ancient successions.

DATA AND METHODS

Two main datasets are used in this research: (i) 39 runs of physics-based numerical models that simulate the formation and evolution of braided rivers (see below for details on the model and on model conditioning), and (ii) statistics of bar dimensions and the braiding degree of 63 modern braided rivers. The statistics of bar dimensions were measured from natural braided river reaches that are relatively pristine or that have only been subjected to limited anthropogenic modifications (Tables A1 and A2 in Supporting Information). For each chosen river reach, time-lapse measurements were obtained for mid-channel bars using satellite images from Google Earth (Fig. 1). Values of gradient for each studied reach were derived from published data or from Google Earth, calculated as the difference in elevation between the reach endpoints and the horizontal distance measured along the sinuous path of the largest channel in the braid belt (cf. Castelltort, 2018; Holzweber *et al.*, 2014).

Numerical modelling outputs consist of records of riverbed topography and bathymetry, sediment concentration, and hydrodynamics. These records are expressed principally as time series data of water depth, water surface elevation, magnitude and rate of riverbed erosion or sedimentation, Froude number, average flow velocity, bed-load transport rate and riverbed grain size. Details of river dynamics, morphology and evolution were extracted from time-lapse plan-view images (ranging from 1000 to 5000 for each model run, depending on the simulation time), with a time interval of 1 hour, and a resolution of 10 m downstream and 5 m across stream (see the model settings below).

Interpretation and analyses of the simulated rivers consisted of the two following main activities. (i) Investigation of the formation of braided rivers and of their accretion through stages of evolution from a planar (featureless) bed. This is undertaken based on both visual and quantitative analyses of time-series data of riverbed geomorphology, hydrodynamics and geometry of river deposits. (ii) Investigation of relationships between morphology of braided rivers and values of gradient, water discharge and river depth. This is undertaken mainly through comparisons between different modelling runs, which were designed to enable analysis of the sensitivity of the model outputs to water discharge, river depth and riverbed gradient. This second main activity was also applied in the analyses of real-world rivers.

In this work, the boundaries delimiting braid bars from adjacent channels on the satellite images were placed either at the transition between flowing water and emergent areas (Fig. 1A), else at the transition between partly vegetated bars and the exposed unvegetated riverbed where this is dry (Fig. 1B). Satellite images that were evidently taken at high flow stage were purposely excluded, and this could be done by comparing multiple acquisitions of satellite images at evidently different flow stages. A similar approach was followed in prior research (e.g. Castelltort, 2018; Kelly, 2006; Schuurman & Kleinhans, 2015). For the modelled braided rivers, the boundaries between bars and channels were placed at the transition between accretion (elevation gain) and erosion (elevation loss) relative to the initial planar bed configuration (Fig. 1C and D) (Baar *et al.*, 2019; Schuurman *et al.*, 2013).

Bar length is defined as the maximum dimension of a mid-channel bar parallel to the river-flow direction; bar width is the maximum dimension perpendicular to the bar-length axis (Fig. 1A) (Kelly, 2006). The bar aspect ratio is used to describe the morphology of braid bars quantitatively, as the ratio between the bar length and the bar width (cf. Kelly, 2006). The term 'channel depth' is defined here as the maximum bankfull depth, i.e. as the thalweg depth at

bankfull discharge, as shown in Fig. 1D; 'mean channel depth' (also termed 'river depth') is the mean value of measured channel depths across multiple cross-stream sections along the same river reach, which are equally spaced by 1 km for the river simulations (see below for section locations); the 'average water depth' is the raster mean of depth values across all grid cells where the riverbed is submerged. The 'bar mode', which serves as an indicator of the degree of braiding, is defined as the number of compound bars per cross-section perpendicular to the channel belt, following Seminara & Tubino (1989).

MODEL DESCRIPTION

Basic formulations for hydrodynamics and sediment transport

In Delft3D, hydrodynamics are based on the three-dimensional (3D) Reynolds-averaged Navier-Stokes equations, derived from conservation of momentum and mass (Caldwell & Edmonds, 2014; Deltares, 2014). Based on a set of assumptions, including shallow water and Boussinesq approximation, the Navier-Stokes equations are simplified as follows:

$$\frac{\partial u}{\partial t} + u\frac{\partial u}{\partial x} + v\frac{\partial u}{\partial y} + w\frac{\partial u}{\partial z} = -g\frac{\partial \zeta}{\partial x} - \frac{gu\sqrt{u^2+v^2}}{C^2 h} + F_x + V_h\left(\frac{\partial^2 u}{\partial x^2} + \frac{\partial^2 u}{\partial y^2}\right) + \frac{\partial}{\partial z}\left(V_V\frac{\partial u}{\partial z}\right) \quad (1)$$

$$\frac{\partial v}{\partial t} + u\frac{\partial v}{\partial x} + v\frac{\partial v}{\partial y} + w\frac{\partial v}{\partial z} = -g\frac{\partial \zeta}{\partial y} - \frac{gv\sqrt{u^2+v^2}}{C^2 h} + F_y + V_h\left(\frac{\partial^2 v}{\partial x^2} + \frac{\partial^2 v}{\partial y^2}\right) + \frac{\partial}{\partial z}\left(V_V\frac{\partial v}{\partial z}\right) \quad (2)$$

$$\frac{\partial (hu)}{\partial x} + \frac{\partial (hv)}{\partial y} + \frac{\partial w}{\partial z} = 0 \quad (3)$$

where t is time, x is the downstream coordinate, y is the lateral coordinate (Fig. 2), z is the vertical coordinate, u is flow velocity in the x-direction, v is flow velocity in the y-direction, w is the flow velocity in the z-direction, ζ is the water level, h is the water depth, C is the Chezy roughness, V_h is the horizontal eddy viscosity, V_V is the vertical eddy viscosity, g is the gravity acceleration constant, and F_x and F_y are the radiation stress

gradients in the x and y directions. Formulas (1) and (2) describe conservation of momentum in the fluid, whereas (3) describes the conservation of mass.

In Delft3D, sediment transport is computed separately for cohesive and non-cohesive fractions. Processes of sediment transport, deposition and erosion are modelled according to the Partheniades-Krone formulation for cohesive sediment fractions (Partheniades, 1965), and following the approach by van Rijn *et al.* (2001) for non-cohesive sediments (Deltares, 2014). When a dry cell in the model grid is adjacent to a wet cell – i.e. at the boundary between flowing water and emergent areas – the amount of erosion is shared equally between the wet and the dry cells (i.e. the factor for erosion of adjacent dry cells is set to 0.5, see Table 1).

Boundary conditions and general settings

Model boundary conditions mainly include grid setting, and flow and transport conditions (Caldwell & Edmonds, 2014; Deltares, 2014). A sloping planar and featureless riverbed with constant width was considered in this work, meaning that no initial river-bed topography was specified (Nicholas *et al.*, 2013; Schuurman *et al.*, 2013). The bed roughness formula of Manning and the K-Epsilon turbulence model were selected. The model domain was set as having an erodible substrate and five vertical layers with equal thickness. Two fixed non-erodible walls were considered for the model domain, in line with prior research (Williams *et al.*, 2016; Schuurman *et al.*, 2013; Schuurman & Kleinhans, 2015); this condition makes the simulations especially relevant to situations where braided rivers are confined within alluvial valleys with walls that resist to erosion over the timescales of the modelled scenarios. The model domain is represented by a grid with a cross-stream width (direction Y) of 1 km and a dip length (direction X) of 10 km; the grid has a resolution of 10 m along X and 5 m along Y (Fig. 2). Mid-channel bars tend to be elongated downstream; therefore, the chosen resolution

optimizes computational speed without significantly affecting accuracy. At the beginning of each run, the longitudinal gradient of the domain, and hence of the riverbed, is uniform, and water discharge is constant. An initial bed level perturbation of 0.01 m is set on the initial riverbed, as was done in prior research (Nicholas *et al.*, 2013; Schuurman & Kleinhans, 2015). This study has also followed the approach proposed by Baar *et al.* (2019) for model optimization, which allows a reduction of unwarranted channel incision that commonly arises as artefact of the simulations. All of the main parameters and their initial settings are shown in Tables 1 and 2.

The gradient of the model domain and the river water discharge are set to vary across different runs. The value of initial gradient increases progressively from group A to group F (Runs 1 to 34), taking values of 0.1 m/km, 0.3 m/km, 0.5 m/km, 1 m/km, 2 m/km and 4 m/km, respectively (Table 2); these values cover a range of gradients typical of natural sand-bed braided rivers (van den Berg, 1995). For each value of riverbed gradient, the input water discharges have been iteratively adjusted so as to obtain modelled rivers that cover the same range of bathymetries (average water depth: 1.6–2.8 m) for any gradient (Runs 1–34). The average water depth is therefore a model result, which is estimated when modelled rivers reach a nearly steady state, i.e. when the bar top surface reaches (or is close to) water level (Fig. 2D). Group G simulations (Runs 35–39) are instead set up as having the same discharge (1600 m^3/s) but progressively increasing slopes (Table 2). In all runs, the riverbed material is composed of non-cohesive (sandy) sediment, with grain sizes following a log-normal distribution ranging from 0.2 mm to 1.0 mm and with a median value of 0.6 mm. Although the grain sizes of the initial bed materials are the same, the grain sizes on the riverbed surfaces are allowed to change during the simulation, as a result of the interaction between the riverbed and the stream flow. Therefore, grain sizes on the riverbed surface are variable across the 39 river simulations.

Sediment (sand) concentration at the upstream boundary of the model, which controls sediment flux, has been adjusted iteratively according to observations of average sediment concentration for the modelled river domain between km 5 and km 6 along the X-direction; this iterative adjustment has been performed for each run so as to achieve conditions of approximately equal input and output sediment flux. This way, the initial riverbed gradient should approximate a graded profile (Caldwell & Edmonds, 2014), and should therefore only vary limitedly during the simulation time.

RESULTS

Formation and morphology of braided rivers from featureless beds

Thirty-nine runs of river modelling were performed; these differed with respect to gradient and water discharge (Table 2). Although there are marked differences in the morphology of the resultant modelled rivers, all simulations underwent similar evolutionary stages: (i) an initial state of flow over a planar surface; (ii) formation of transverse, lobate unit bars (Fig. 3B; cf. natural examples in Fig. 3H), which then commenced downstream migration; (iii) channelization developing around unit bars (for example, bars B and C in Fig. 3B; cf. bar 1 in natural example in Fig. 3I), and in some cases dissection of unit bars by new channels (for example, bars E and F in Fig. 3B; cf. bar 2 in natural example in Fig. 3I), in parallel with deposition of bar-tail limbs (for example, bars B and C in Fig. 3B; cf. natural examples in Fig. 3J); (iv) formation of compound bars by coalescence of unit bars (for example, bar D in Fig. 3C; cf. natural examples in Fig. 3J); and (v) amalgamation of relatively simpler compound bars into larger and more complex compound bars forming river islands, via progressive channel abandonment (for example, Islands 1 in Fig. 3F, and larger compound bars in Fig. 3L). The characteristics of all these evolutionary stages recognized in the river simulations are

effectively observable in natural braided rivers. Eventually, the braided rivers reach a nearly steady configuration, a state of dynamic equilibrium in which the compound bar surface reaches or is close to the water level, and channel morphodynamics continue in a way whereby the geometric characteristics of barforms and channels remain approximately stationary through time (Fig. 3E and F). For example, the modelled rivers show different morphologies at 2000 and 4000 days, but the types and geometric characteristics of the morphologies are entirely comparable (for example, compare Fig. 3E and 3F). The evolutionary stages of the modelled braided rivers can be summarized into four stages, as shown in Fig. 4. In the earliest stage of the simulation, unit bars have limited relief and only modest channelization has developed. At the second stage, unit bars tend to coalesce to form initial compound bars that are more clearly demarcated by the developing network of channels. At the third stage, compound bars grow further by unit-bar accretion and amalgamation. At the last stage, the simulated rivers reach a nearly steady state with slower rates of morphodynamic change.

Amalgamated compound bars and their development

'Complex' compound bars are braid bars that originated from the amalgamation of multiple simpler compound bars and unit bars (Fig. 5). The evolution of these bars can be summarized into three stages: (i) migration and development of unit bars; (ii) amalgamation of unit and compound bars; and (iii) channel infill between compound bars.

Initially, unit bars tend to migrate more rapidly than compound bars, because of the significant water columns on their top (Fig. 3) (Nicholas *et al.*, 2013; Williams *et al.*, 2013). As they migrate, unit bars grow and develop into compound bars (Fig. 5A and B). Subsequently, unit bars can amalgamate with compound bars occurring downstream, because of their different migration rates (Fig. 5B and C). As a result, channel branches between the bars become

narrower and shallower (cf. CB-1 to CB-5 in Fig. 5C). Afterwards, these shallower channels tend to aggrade further, because they are traversed by slower flows compared to larger river branches, and are therefore ultimately infilled. Transient variations in near-bed sediment concentration act as an indicator of the state of evolution of bars and channels: a downstream increase in sediment concentration indicates that bed material is being eroded and transported, whereas a downstream decrease suggests that deposition is occurring, and the latter situation is seen in branches that are being plugged during the assemblage of larger compound bars (cf. CB-1 to CB-5; Fig. 5C and D). As a result, complex compound bars are generated (Fig. 5E) that are similar to those seen in real-world braided rivers (Fig. 5F and G).

Morphology of braided rivers and geometry of their deposits

Relationships with riverbed gradient

The riverbed gradient is not an independent parameter in fluvial systems, since it adjusts naturally to water discharge, and rate and calibre of sediment supply (Ashworth & Lewin, 2012; Baar *et al.*, 2019; Smith *et al.*, 2006; Simpson & Castelltort, 2012). Iterative adjustment of inputs and outputs of liquid and solid discharges was undertaken to attain conditions of near equilibrium. Nevertheless, the long profiles of the modelled rivers underwent some changes through the simulation time, which indicates that the simulated streams were not perfectly at grade at the outset of the model runs. For example, the initial forced riverbed gradient of Run 10 was set as 0.3 m/km; the average streambed gradient was 0.29 m/km at the simulation time when the modelled river reached a state of dynamic equilibrium in planform development (Fig. 6). The gradient changes experienced by the 39 modelled rivers were calculated; the absolute values of relative changes in longitudinal gradient were in most cases (35 rivers of the 39) less than 6% of the initial gradients (Fig. 6D and E).

Measurements of bar area, bar height and bar length-to-width ratio are based on compound braid bars, whose boundaries were placed at the transition with active channels. Across the 39 runs, as the riverbed gradient increases while the water discharge is maintained constant, the depth-averaged flow velocity increases, the average water depth decreases, compound-bar areas and heights decrease (Fig. 7), and the mean bar mode (i.e. the mean value of measurements of bar mode across nine cross-sections as shown in Fig. 7) increases. For example, for runs conducted with a discharge of 1600 m^3/s, as the gradient increases from 0.1 m/km to 2.0 m/km, the average water depth decreases from 3.00 m to 1.35 m; bar areas and heights, also decrease markedly, whereas the mean bar mode increases sharply (Fig. 7).

Notably, most compound bars are elongated downstream, and their aspect ratios (length-to-width ratio) tend to increase with the gradient (Fig. 8). This observation is in accord with observations from natural rivers made in this work and in previous research (Crosato & Mosselman, 2009; Castelltort, 2018). In the Buha River, China (Fig. 8A), for example, reaches with similar discharge (zone 1 to zone 3 in Fig. 8A) demonstrate that a decreasing gradient is associated with an increase in bar area, a reduction in bar aspect ratio, and a decrease in bar mode (Fig. 8B to D).

Relationships with water discharge

For conditions of fixed slope but variable discharge, bar areas and heights tend to increase with increasing discharge, whereas the bar mode instead decreases on average (Fig. 9). Specifically, as the water discharge increases from 1370 m^3/s to 3080 m^3/s, the average bar area increases from 43500 m^2 (Fig. 9A) to 120500 m^2 (Fig. 9C), and the mean bar mode decreases from 6.2 to 4.1. These observations are made on simulations for which a constant steady discharge was considered, which can be treated as a bed-forming discharge

approximating the bankfull discharge of natural rivers, in accord with prior research (e.g. Rossi *et al.*, 2016; Schuurman *et al.*, 2013; Schuurman & Kleinhans, 2015, Williams *et al.*, 2016).

Relationships with river depth

Observations on the modelled rivers indicate that bar areas and heights correlate positively with the river depth, relative to which they may be scaled primarily. As shown in Fig. 10, the modelled rivers have similar river depths (varying between 7.0 m and 7.2 m), and although they differ markedly with respect to gradients and discharges, they do not show significant differences in mean bar areas and heights.

Quantitative relationships with gradient and water discharge

To gain an improved understanding of the significance of relationships between bar geometry, bar mode, riverbed gradient and flow discharge, outputs produced by the 39 runs are analysed as shown in Fig. 11, in which all the parameters above were measured when compound bar surfaces reached the water level at the river output, as shown in Fig. 3E. Coefficients of variation (ratios of standard deviation to mean) of braid-bar area and length-to-width ratio of 39 modelled rivers shown in the box plots (Fig. 11) are reported in Table 3.

These data indicate that bar areas are correlated positively with discharge for a fixed gradient (runs 1 to 35 in Fig. 11A), and negatively with the gradient for a fixed discharge (runs 35 to 39 in Fig. 11A). Moreover, the bar area shows a strong positive relationship with water depth (Fig. 11A and B, $R^2 = 0.95$). The mean values of bar area are similar across different runs having the same average water depths (coefficients of variation are less than 0.2, see Fig. 11B), regardless of the input values of bed gradient and discharge. Mean values of bar aspect ratio (length-to-width ratio) are correlated positively with bed gradient across the 39 runs, regardless of the input water discharge (Fig. 11C and D, $R^2 = 0.92$).

In view of the direct proportionality between bar area and river depth (Fig. 10), quantitative relationships between channel depths and bar areas were determined for both the 39 modelled rivers (Fig. 11B, $R^2 = 0.95$) and 24 real-world river reaches; in both datasets, a strong positive correlation between these two variables was observed (Fig. 11G, $R^2 = 0.96$).

Since earlier research (Parker, 1976; Crosato & Mosselman, 2009) has shown that the bar mode correlates positively with the river width-to-depth ratio (ratio of river width to river depth), relationships between bar mode and river width-to-depth ratio are determined in this work (Fig. 11F). The results indicate that in the modelled rivers the bar mode correlates positively with: (i) the river width-to-depth ratio for a given riverbed gradient; and (ii) with the riverbed gradient for the same river width-to-depth ratio. Corresponding relationships have been recognized in the 44 studied real-world river reaches (Fig. 12A and B). Consideration of the riverbed gradient yields improved prediction of mean bar mode, relative to the empirical relationship based on width-to-depth ratio alone (coefficients of determination of 0.89 and 0.84, respectively).

SUMMARY: APPLICATIONS AND LIMITATIONS

Influence of river depth and bed gradient on braided-river morphology

An increase in riverbed gradient results in increasing flow velocity and energy, which tends to inhibit accretion of mid-channel bars on their sides (Claude *et al.*, 2014); this results in an increase in bar length-to-width ratio (Castelltort, 2018), and is recorded in the observed positive relationship between gradient and compound bar length-to-width ratio (Fig. 10C and D).

There are at least two reasons why the gradient has a significant effect on bar mode. Primarily, the riverbed gradient influences the bar mode because steeper riverbeds are

commonly associated with more elongated mid-channel bars, whereas rivers with gentler slopes tend to exhibit broader bars. Furthermore, the bar mode tends to increase with width-to-depth ratio. It should however be noted that the riverbed gradient is genetically related to the river width-to-depth ratio (Holbrook & Schumm, 1999; Crosato & Mosselman, 2009), because an increased gradient tends to be associated with larger flow rate and shallower river depth, thereby commonly resulting in a larger width-to-depth ratio and a relatively less stable channel belt (Ouchi, 1985).

Compound bar areas correlate positively with discharge for a fixed gradient, and negatively with gradient for a fixed discharge (Figs 7 to 9). Again it must be noted that the riverbed gradient and the water discharge are both genetically related to the river depth (Parker *et al.*, 2007; Ashworth & Lewin, 2012). In particular, the 39 modelled rivers are set as having the same initial bed material; as such, the river depth is related positively to discharge, and negatively to bed gradient. Observations on the 39 modelled rivers and 24 real-world rivers indicate that there is a strong positive correlation between the bar area and the river depth, even across markedly different values of gradient and discharge (Fig. 11G). This indicates that the bar area is primarily scaled to the river depth, whose relationships can be expressed in Eq. 4:

$$A = (8.3H)^{2.78} \quad (R^2 = 0.96) \tag{4}$$

where A is the mean compound bar area of a river reach [m^2] and H is the river depth for that reach [m]. This proposed relationship is also compared to the data reported by Kelly (2006), which show a similar trend (Fig. 11G).

Quantitative relationships for empirical predictions

As illustrated in Figs 11G and 12B, empirical relationships between: (i) compound bar area and river depth (Eq. 4); and (ii) between bar mode, riverbed gradient and river width-to-

depth ratio are established (Eq. 5). Also, empirical equations are established between bar area and river depth (Eq. 6), and for predicting the riverbed gradient based on bar mode and river width-to-depth ratio (Eq. 7).

The empirical relationships presented in Eqs 4 and 6 are established through regression analysis of data from 39 modelled rivers and 24 real-world river reaches (Fig. 11G); the applicability of these relationships is substantiated by comparison with the corresponding relationship reported by Kelly (2006; Fig. 11G). Instead, the relationship in Eq. 5 is obtained based on the combination of the following empirical findings: (i) in model runs with the same river depth, the bar mode is proportional to $G^{0.19}$, where G is the river slope; (ii) in model runs with the same river slope, the bar mode is proportional to $(\frac{B}{H})^{0.9}$, where B is the river width and H is the river depth. Eqs 4 to 7 are therefore proposed as tools for predicting characteristics of braided channel-belt morphology, as follows:

$$M = 0.041\ (B/H)^{0.9} * G^{0.19} \quad (R^2 = 0.88) \tag{5}$$

$$H = 0.153A^{0.341} \quad (R^2 = 0.95) \tag{6}$$

$$G = (\frac{21M}{(B/H)^{0.9}})^{4.3} \quad (R^2 = 0.70) \tag{7}$$

where, for a given river reach, A is the mean compound bar area [m^2], H is the river depth [m], B is the river width [m], M is the mean bar mode and G is the mean riverbed gradient [m/km].

To demonstrate the predictive power of Eqs 5 and 7, cross-plots of estimated versus observed values of bar-mode and longitudinal gradient are presented in Fig. 13A and 13B, respectively, for 44 real-world river reaches. Error analyses are also presented in Fig. 13C and 13D. The mean absolute error of estimated bar modes is approximately 0.75, and the

absolute discrepancy is less than two for almost all cases (42 of 44) (Fig. 13C). Similarly, the mean absolute error of estimated longitudinal gradients is approximately 2.0 m/km after two rivers were excluded from the statistical analysis. These results support the general predictive value of the empirical relationships proposed for inference of bar mode and riverbed gradient.

Applications to modern rivers and ancient successions

Compound bar area and channel depth

Channel depth and bar area are both common morphological parameters employed to describe fluvial systems (Kelly, 2006). However, there are situations where constraining both parameters is not possible, for example in cases where: (i) planform characteristics of the formative rivers of preserved channel-belt deposits cannot be reconstructed from their direct observation in fluvial strata (for example, in outcrop or well logs) (Li *et al.*, 2015; Yao *et al.*, 2018); (ii) where bathymetric surveys of modern rivers are lacking (Smith *et al.*, 2006; Miall, 2011); or (iii) where 3D seismic data of subsurface fluvial successions allow imaging of preserved abandoned mid-channel bars in planform but channel-fill thicknesses are below the vertical seismic resolution (cf. Zhuo *et al.*, 2015).

Therefore, the quantitative relationships shown in Eqs. 4 and 6 could be applied for the following purposes: (i) to predict channel depth for modern fluvial systems in which mean bar area can be readily measured, for example using remote-sensing datasets (Castelltort, 2018), but direct bathymetric data are not available; Eq. 6; (ii) to predict bar areas – and hence help reconstruct formative channel-belt geometry – for subsurface successions in which channel depth could be inferred by sedimentological analyses of outcrops, cores or well logs; Eq. 4; and to (iii) predict channel-fill thicknesses or the depth of formative channels of subsurface

successions in which bar areas can be mapped in planform (Ethridge & Schumm, 2007; Bellwald *et al.*, 2021).

Bar mode and riverbed gradient

The bar mode is a morphological parameter for braided rivers, which is also applied to discriminate braided from single-thread river patterns (Parker, 1976; Crosato & Mosselman, 2009). The relationship presented in Eq. 5 provides a simple yet effective predictive tool for estimating the bar mode of the formative rivers of ancient successions for which hydraulic geometry and gradient can be estimated (Ganti *et al.*, 2019; Greenberg *et al.*, 2021; Long, 2021). This approach can thus be employed to attempt a quantification of the degree of braiding of the formative rivers of fluvial successions. The relationship in Eq. 5 can also be used to predict morphological responses to changes in river width and depth resulting from river engineering, such as channel-belt widening undertaken to reduce flooding risk (Crosato & Mosselman, 2009), or from changes in bed gradient imposed by active tectonics (Ouchi, 1985; Roy & Sahu, 2015).

Previous research (Parker, 1976; Parker *et al.*, 2007; Crosato & Mosselman, 2009) state that the river width-to-depth ratio is the parameter that is most strongly associated with the bar mode, such that the bar mode can be considered primarily as a function of the river width-to-depth ratio. However, this work demonstrates that consideration of the riverbed gradient in the regression analysis results in increased predictive power (Fig. 11B); hydraulic roughness and river sediment transport rate which also have effects on bar mode (Parker, 1976; Parker *et al.*, 2007), are ignored, but determining these for rivers at bankfull conditions is difficult (Ahmed & Saad, 1992; Smith *et al.*, 2006; Baar *et al.*, 2018), as is their inference from preserved deposits in ancient fluvial successions (Fielding *et al.*, 2018). Nevertheless, the predictive

power of the proposed relationship may in part reflect how the river width-to-depth ratio and riverbed gradient are themselves related to, among other morphodynamic parameters, hydraulic roughness and its effect on sediment transport (Smith *et al.*, 2006; Ashworth & Lewin, 2012; Simpson & Castelltort, 2012).

The relationship presented in Eq. 7 can particularly be applied to the estimation of the bed gradient of braided rivers whose deposits are preserved in fluvial successions, in cases where the bar mode and the river width-to-depth ratio can be inferred. For example, the bar mode and river width-to-depth ratio may be inferred based on observations made in outcrop (Li *et al.*, 2020), else estimated in subsurface fluvial successions for which 3D seismic data and well data are both available (Li *et al.*, 2019). Therefore, this relationship can be applied to assist palaeohydrological reconstructions of ancient fluvial strata that rely on gradient (slope) estimates (cf. Long, 2021, and references therein). Such estimates are fundamental for the inference of depositional processes, magnitude of sediment flux, and bedform characteristics, among other things (Smith *et al.*, 2006; Holbrook & Wanas, 2014; Mahon & McElroy, 2018).

Limitations

In this work, each numerical model was set as having constant flow discharge and no vegetation, which means that the effects of discharge variability and vegetation were neglected. In natural braided rivers, vegetation contributes to the stabilization of banks and bars (Nicholas *et al.*, 2013), and discharge variability plays an important role on controlling the riverbed reworking and preservation of sediment bodies (Edmonds & Slingerland, 2008; Fielding *et al.*, 2018; Limaye, 2020). Therefore, it would be prudent to exclusively apply the proposed relationships to river systems characterized by limited discharge variability and vegetation density. Also, the modelled rivers were set as confined by fixed non-erodible walls following

the approach taken in some prior research (Schuurman *et al.*, 2013; Schuurman & Kleinhans, 2015; Williams *et al.*, 2016); as such the results may not necessarily be applicable to freely wandering natural braided rivers limited by highly erodible substrates. Nonetheless, our comparison between the predicted and observed values of bar mode and streambed gradient demonstrates that general estimations of bar mode and streambed gradient can be attempted by using the proposed relationships (Fig. 13).

In addition, the modelled rivers exhibit unexpected channel incision as an artefact of the simulations, resulting from an imbalance between non-linearity of downstream sediment transport that leads to channel erosion and transverse sediment transport, which counteracts incision (Baar *et al.*, 2019). Grid cell size is the primary factor controlling this imbalance, and the resulting channel incision. In Delft3D, water flow tends to occur through the smallest possible number of grid cells; hence, a smaller cell size can cause a larger water discharge locally, resulting in enhanced local erosion. The cell size was chosen as 5 m × 10 m, making the resolution of the grid higher than that of most comparable studies using Delft3D (cf. Crosato *et al.*, 2011; Nicholas *et al.*, 2013; Schuurman *et al.*, 2013); nonetheless, the degree of channel incision is negligible for the scopes of this study (see Fig. S1 in supplementary files).

In the application of the presented empirical tools, it must be considered that important spatial variability may exist in braid-bar planform areas, length-to-width ratio and bar mode in the same river reach. Therefore, robust applications of Eqs 4 to 7 should be based on mean values of these variables that are underpinned by multiple observations from the same river reach. A general word of caution should also be made regarding the possible application of the proposed relationships (Eqs 4 to 7) to the stratigraphic record of braided rivers, since the geometry of barform architectural elements that record the morphodynamic evolution of braid bars can be significantly different from the morphologies of the formative landforms, in part

due to the effect of partial preservation in determining the geometry of the deposits that are ultimately preserved (cf. Chamberlin & Hajek, 2019; Greenberg *et al.*, 2021).

CONCLUSIONS

Based on 39 numerical simulations of braided rivers produced using Delft3D numerical modelling software, and the analysis of the form of 63 real-world braided rivers, the following novel findings arise.

1 Under constant discharge, the development of a braided river from a planar featureless bed includes four stages: (i) formation of transverse unit bars; (ii) channelization; (iii) formation of compound bars; and (iv) amalgamation of relatively simpler compound bars into more complex compound bars. Eventually, the simulated rivers reach a nearly steady state (or a dynamic equilibrium) with a slower evolution rate and temporally stationary morphological characteristics.

2 The morphology of the modelled braided rivers is related to the riverbed gradient, flow discharge and mean river depth: (i) bar heights and areas are scaled positively with flow discharge and negatively with bed gradient; (ii) the bar length-to-width aspect ratio exhibits a positive relationship with riverbed gradient; (iii) the bar mode (degree of braiding) correlates directly with both river width-to-depth ratio and riverbed gradient.

3 The bar area is primarily correlated with the river depth in a braided-river reach. A quantitative relationship between the mean bar area and river depth is established, for the braided-river reaches, which provides a predictor for bar areas or channel depth in braided rivers. This relationship can be applied in remote-sensing studies of modern rivers and to infer the palaeogeomorphology and palaeohydraulics of fluvial successions. Given that the possible

roles of discharge variability and vegetation were ignored, the proposed relationship is suited for application to rivers with limited discharge variations and that lack densely vegetated banks.

4 A quantitative relationship for predicting the bar mode from the river width-to-depth ratio and riverbed gradient is proposed. This relationship can be applied to infer the likely planform of the formative braided rivers of fluvial successions, to infer streambed gradients for scopes of palaeohydrological reconstructions, and to assess effects of changes in river width resulting from river engineering, or from changes in bed gradient imposed by active tectonics. Nonetheless, the proposed relationships only allow prediction of braid-bar morphologies as geomorphic entities; these are rarely preserved as such in the stratigraphy of braided rivers, due inherent morphodynamics and preservation potential.

ACKNOWLEDGEMENTS

This research was financially supported by the National Natural Science Foundation Project of China (No. 41872107), the China National Postdoctoral Science Foundation (2022M713458), and Cooperation Project of the PetroChina Corporation (ZLZX2020-02). LC and NPM thank the sponsors and partners of FRG-ERG-SMRG for financial support: AkerBP, Areva (now Orano), BHPBilliton, Cairn India (Vedanta), ConocoPhillips, Chevron, Equinor, Murphy Oil, Nexen-CNOOC, Occidental, Petrotechnical Data Systems, Saudi Aramco, Shell, Tullow Oil, Woodside and YPF. Gary Weissmann, Sebastien Castelltort, an anonymous reviewer, and Associate Editor Charlie Bristow are thanked for their constructive comments, which helped improve the article.

REFERENCES

Ahmed, S.E. and **Saad, M.B.** (1992) Prediction of natural channel hydraulic roughness. *J. Irrig. Drain. Eng.*, **118**, 632–639.

Ashworth, P.J. and **Lewin, J.** (2012) How do big rivers come to be different? *Earth-Science Rev.*, **114**, 84–107.

Baar, A.W., **Boechat Albernaz, M.**, **van Dijk, W.M.** and **Kleinhans, M.G.** (2019) Critical dependence of morphodynamic models of fluvial and tidal systems on empirical downslope sediment transport. Nat Commun. doi: 10.1038/s41467-019-12753-x

Baar, A.W., **de Smit, J.**, **Uijttewaal, W.S.J.** and **Kleinhans, M.G.** (2018) Sediment Transport of Fine Sand to Fine Gravel on Transverse Bed Slopes in Rotating Annular Flume Experiments. *Water Resour. Res.*, **54**, 19–45.

Bellwald, B., **Planke, S.**, **Polteau, S.**, **Lebedeva-Ivanova, N.**, **Faleide, J.I.**, **Morris, S.M.**, **Morse, S.** and **Castelltort, S.** (2021) Characterization of a glacial paleo-outburst flood using high-resolution 3-D seismic data: Bjornelva River Valley, SW Barents Sea. *J. Glaciol.*, **67**, 404–420.

Bernini, A., **Caleffi, V.** and **Valiani, A.** (2006) Numerical Modelling of Alternate Bars in Shallow Channels. In: *Braided Rivers* (Ed. G.H.S. Smith, J.L. Best, C.S. Bristow, G.E. Petts, and I. Jarvis), *Blackwell*, Oxford, 153–175.

Smith, G.H.S., Best, J.L., **Bristow, C.S.** and **Petts, G.E.** (2006) Braided Rivers: Process, Deposits, Ecology and Management. *Blackwell*, Oxford, 390 pp.

Bridge, J.S. and **Lunt, I.A.** (2006) Depositional Models of Braided Rivers. In: *Braided Rivers* (Ed. G.H.S. Smith, J.L. Best, C.S. Bristow, G.E. Petts, and I. Jarvis), *Blackwell*, Oxford, 11–50.

Bridge, J.S., **Smith, N.D.**, **Trent, F.**, **Gabel, S.L.** and **Bernstein, P.** (1986) Sedimentology and morphology of a low-sinuosity river: Calamus River, Nebraska Sand Hills. *Sedimentology*, **33**, 851–870.

Caldwell, R.L. and **Edmonds, D.A.** (2014) Delft3D-Flow: Simulation of Multi-Dimensional Hydrodynaminc Flows and Transport Phenomena, Including Sediments-User Manual. *J. Geophys. Res. Earth Surf.*, **119**, 961–982.

Castelltort, S. (2018) Empirical relationship between river slope and the elongation of bars in braided rivers: A potential tool for paleoslope analysis from subsurface data. *Mar. Pet. Geol.*, **96**, 544–550.

Chamberlin, E.P. and **Hajek, E.A.** (2019) Using bar preservation to constrain reworking in channel-dominated fluvial stratigraphy. *Geology*, **47**, 531–534.

Claude, N., **Rodrigues, S.**, **Bustillo, V.**, **Bréhéret, J.G.**, **Tassi, P.** and **Jugé, P.** (2014) Interactions between flow structure and morphodynamic of bars in a channel expansion/contraction, Loire River, France. *Water Resour. Res.*, **50**, 2850–2873.

Crosato, A. and **Mosselman, E.** (2009) Simple physics-based predictor for the number of river bars and the transition between meandering and braiding. *Water Resour. Res.*, **45**, 1–14.

Crosato, A. and **Saleh, M.S.** (2011) Numerical study on the effects of floodplain vegetation on river planform style. *Earth Surf. Process. Landforms*, **36**, 711–720.

Deltares (2014) Delft3D-Flow: Simulation of Multi-Dimensional Hydrodynaminc Flows and Transport Phenomena, Including Sediments-User Manual. Delft, Netherlands, 688 pp.

Edmonds, D.A. and **Slingerland, R.L.** (2008) Stability of delta distributary networks and their bifurcations. *Water Resour. Res.* **44**, 1–13. https://doi.org/10.1029/2008WR006992

Ethridge, F.G. and **Schumm, S.A.** (2007) Fluvial seismic geomorphology: A view from the surface. *Geol. Soc. Spec. Publ.*, **277**, 205–222.

Fielding, C.R., **Alexander, J.** and **Allen, J.P.** (2018) The role of discharge variability in the formation and preservation of alluvial sediment bodies. *Sediment. Geol.*, **365**, 1–20.

Ganti, V., **Whittaker, A.C.**, **Lamb, M.P.** and **Fischer, W.W.** (2019) Low-gradient, single-threaded rivers prior to greening of the continents. *Proc. Natl. Acad. Sci. U. S. A.*, **116**, 11652–11657.

Greenberg, E., **Ganti, V.** and **Hajek, E.** (2021) Quantifying bankfull flow width using preserved bar clinoforms from fluvial strata. *Geology*, **49**, 1038–1043.

Holbrook, J. and **Schumm, S.A.** (1999) Geomorphic and sedimentary response of rivers to tectonic deformation: A brief review and critique of a tool for recognizing subtle epeirogenic deformation in modern and ancient settings. *Tectonophysics*, **305**, 287–306.

Holbrook, J. and **Wanas, H.** (2014) A Fulcrum Approach To Assessing Source-To-Sink Mass Balance Using Channel Paleohydrologic Paramaters Derivable From

Common Fluvial Data Sets With An Example From the Cretaceous of Egypt. *J. Sediment. Res.*, **84**, 349–372.

Holzweber, B.I., **Hartley, A.J.** and **Weissmann, G.S.** (2014) Scale invariance in fluvial barforms: Implications for interpretation of fluvial systems in the rock record. *Pet. Geosci.*, **20**, 211–224.

Kelly, S. (2006) Scaling and Hierarchy in Braided Rivers and their Deposits: Examples and Implications for Reservoir Modelling. In: *Braided Rivers* (Ed. G.H.S. Smith, J.L. Best, C.S. Bristow, G.E. Petts, and I. Jarvis), *Blackwell*, Oxford, 75–106.

Kleinhans, M.G., **van Dijk, W.M.**, **van de Lageweg, W.I.**, **Hoyal, D.C.J.D.**, **Markies, H.**, **van Maarseveen, M.**, **Roosendaal, C.**, **van Weesep, W.**, **van Breemen, D.**, **Hoendervoogt, R.** and **Cheshier, N.** (2014) Quantifiable effectiveness of experimental scaling of river- and delta morphodynamics and stratigraphy. *Earth-Science Rev.*, **133**, 43–61.

Li, S., **Yu, X.**, **Chen, B.** and **Li, S.** (2015) Quantitative characterization of architecture elements and their response to base-level change in a sandy braided fluvial system at a mountain front. *J. Sediment. Res.*, **85**, 1258–1274.

Li, W., **Yue, D.**, **Colombera, L.**, **Mountney, N.P.** and **Wu, S.** (2020) A novel method for estimating sandbody compaction in fluvial successions. *Sediment. Geol.*, **404**, 105675.

Li, W., **Yue, D.**, **Wu, S.**, **Wang, W.**, **Li, J.**, **Wang, W.** and **Tian, T.** (2019) Characterizing meander belts and point bars in fluvial reservoirs by combining spectral decomposition and genetic inversion. *Mar. Pet. Geol.*, **105**, 168–184.

Limaye, A.B. (2020) How Do Braided Rivers Grow Channel Belts? *J. Geophys. Res. Earth Surf.*, **125**, 1–24.

Long, D.G.F. (2021) Trickling down the paleoslope: an empirical approach to paleohydrology. *Earth-Science Rev.*, **220**, 103740.

Mahon, R.C. and **McElroy, B.** (2018) Indirect estimation of bedload flux from modern sand-bed rivers and ancient fluvial strata. *Geology*, **46**, 579–582.

Miall, A.D. (2011) The Geology of Fluvial Deposits: Sedimentary Sedimentary Facies, Basin Analysis, and Petroleum Geology. *Springer Berlin Heidelberg*, New York, 1689–1699 pp.

Murray, A.B. and **Paola, C.** (1994) A cellular model of braided rivers. *Nature*, **371**,54–57.

Nicholas, A.P., **Ashworth, P.J.**, **Sambrook Smith, G.H.** and **Sandbach, S.D.** (2013) Numerical simulation of bar and island morphodynamics in anabranching megarivers. *J. Geophys. Res. Earth Surf.*, **118**, 2019–2044.

Ouchi, S. (1985) Response of alluvial rivers to slow active tectonic movement. *Geol. Soc. Am. Bull.*, **96**, 504–515.

Parker, G. (1976) On the cause and characteristic scales of meandering and braiding in rivers. *J. Fluid Mech.*, **76**, 457–480.

Parker, G., **Wilcock, P.R.**, **Paola, C.**, **Dietrich, W.E.** and **Pitlick, J.** (2007) Physical basis for quasi-universal relations describing bankfull hydraulic geometry of single-thread gravel bed rivers. *J. Geophys. Res. Earth Surf.*, **112**, 1–21.

Partheniades, E.A. (1965) Erosion and Deposition of Cohesive Soils. *J. Hydraul.*, **91**, 105–139.

Rice, S.P., **Church, M.**, **Wooldridge, C.L.** and **Hickin, E.J.** (2009) Morphology and evolution of bars in a wandering gravel-bed river; lower Fraser river, British Columbia, Canada. *Sedimentology*, **56**, 709–736.

Rossi, V.M., Kim, W., López, J.L., Edmonds, D., Geleynse, N., Olariu, C., Steel, R.J., Hiatt, M. and Passalacqua, P. (2016) Impact of tidal currents on delta-channel deepening, stratigraphic architecture, and sediment bypass beyond the shoreline. *Geology*, **44**, 927–930.

Roy, S. and **Sahu, A.S.** (2015) Quaternary tectonic control on channel morphology over sedimentary low land: A case study in the Ajay-Damodar interfluve of Eastern India. *Geosci. Front.*, **6**, 927–946.

Schumm, S.A. (1985) Patterns of alluvial rivers. *Annual Review of Earth and Planetary Sciences,* **13**,5–27.

Schuurman, F. and **Kleinhans, M.G.** (2015) Bar dynamics and bifurcation evolution in a modelled braided sand-bed river. *Earth Surf. Process. Landforms*, **40**, 1318–1333.

Schuurman, F., **Marra, W.A.** and **Kleinhans, M.G.** (2013) Physics-based modeling of large braided sand-bed rivers: Bar pattern formation, dynamics, and sensitivity. *J. Geophys. Res. Earth Surf.*, **118**, 2509–2527.

Seminara, G. and **Tubino, M.** (1989) Alternate bars and meandering: Free, forced and mixed interactions. In: *River Meandering*, 1st edn. (Ed. S. Ikeda and G. Parker), *American Geophysical Union*, Washington, D. C., 12, 267–320.

Simpson, G. and **Castelltort, S.** (2012) Model shows that rivers transmit high-frequency climate cycles to the sedimentary record. *Geology*, **40**, 1131–1134.

Smith, N.D. (1974) Sedimentology and Bar Formation in the Upper Kicking Horse River, a Braided Outwash Stream. *J. Geol.*, **82**, 205–223.

Stecca, G., **Zolezzi, G.**, **Hicks, D.M.** and **Surian, N.** (2019) Reduced braiding of rivers in human-modified landscapes: Converging trajectories and diversity of causes. *Earth-Science Rev.*, **188**, 291–311.

Sun, J., **Lin, B.** and **Yang, H.** (2015) Development and application of a braided river model with non-uniform sediment transport. *Adv. Water Resour.*, **81**, 62–74.

van den Berg, J.H. (1995) Prediction of alluvial channel pattern of perennial rivers. *Geomorphology*, **12**, 259–279.

van Rijn, L.C., **Roelvink, J.A.A.** and **ter Horst, W.** (2001) Approximation formulae for sand transport by currents and waves. *Deltares*, Delft, 39 pp.

Williams, R.D., **Brasington, J.**, **Hicks, M.**, **Measures, R.**, **Rennie, C.D.** and **Vericat, D.** (2013) Hydraulic validation of two-dimensional simulations of braided river flow with spatially continuous aDcp data. *Water Resour. Res.*, **49**, 5183–5205.

Williams, R.D., **Brasington, J.** and **Hicks, D.M.** (2016) Numerical Modelling of Braided River Morphodynamics: Review and Future Challenges. *Geography Compass*, **10**, 102–127.

Yao, Z., **Yu, X.**, **Shan, X.**, **Li, S.**, **Li, S.**, **Li, Y.**, **Tan, C.** and **Chen, H.** (2018) Braided–meandering system evolution in the rock record: Implications for climate control on the Middle–Upper Jurassic in the southern Junggar Basin, north-west China. *Geol. J.*, **53**, 2710–2731.

Zhuo, H., **Wang, Y.**, **Shi, H.**, **He, M.**, **Chen, W.**, **Li, H.**, **Wang, Y.** and **Yan, W.** (2015) Contrasting fluvial styles across the mid-Pleistocene climate transition in the northern shelf of the South China Sea: Evidence from 3D seismic data. *Quat. Sci. Rev.*, **129**, 128–146.

LIST OF FIGURE AND TABLE CAPTIONS

Fig. 1. Practical approach followed for placing the boundary between bars and channels. (A) Aerial photograph of the Songhua River, China (45°13'59"N, 43'10"E), at low flow stage. (B) Aerial photograph of the Songhua River, China (45° 3'25"N, 124°59'21"E), presenting a mid-channel bar adjacent to channels with dry beds. Sandy channel beds are lighter coloured, whereas the vegetated bar appears darker. (C) Map of the amount of erosion and sedimentation of the riverbed of a modelled river, relative to the initial planar surface. The boundaries of two bars (labelled as 'Bar A' and 'Bar B') are shown as examples. (D) Cross-section of Line A in part (C).

Fig. 2. Boundary and grid setting of the braided-river model (plan view). The upstream and downstream boundaries of the model, and the direction of river flow, are indicated. The model grid is bounded by non-erodible walls. Grid-cell size is 10 m along X (downstream) and 5 m along Y (cross-stream).

Fig. 3. Maps of topography time series and flow velocity of a selected simulation, and satellite image of a natural braided river. (A) to (F) Time series of maps of riverbed erosion and sedimentation, showing an example (Run 10, with an initial gradient of 0.3 m/km and discharge of 1780 m^3/s) of the development and evolution of a braided river from a planar surface. (G) Map of water depth at 2000 days for the same example (Run 10). The simulation time shown in the top-right corner has been corrected by its morphological timescale factor (96x). (H) and (I) Satellite image part of the Sone river in India, which are comparable to the stage of lobate unit bar formation in the modelled rivers (Zone 1 of part B), and to the stage of bar channelization. (J) Satellite image part of the Ganges river in India, showing simpler compound bars with bar-tail limbs and displaying similar features as those seen in the modelled rivers (for example, bars B and C in figure part C). (K) Comparison between the

bed surfaces on 1760 days and on 2000 days, at Section 1 in parts E and F. (L) Satellite image of part of the Brahmaputra in Bangladesh, displaying similar features as those seen in the modelled rivers.

Fig. 4. Summary diagram of modes of evolution of braid bars, including four stages. (A) Unit bars with limited relief and modest channelization. (B) Unit bars evolve into initial compound bars. (C) Compound bars accrete further by unit-bar growth and amalgamation. (D) A nearly steady state with a slower rate of morphodynamic change. Three modes of development of compound bars from unit bars are shown: (i) progressive growth of unit bars into simple compound bars (Bar A); (ii) unit-bar dissection, migration and amalgamation to form simple compound bars (Bars B, C and D); (iii) amalgamation of multiple smaller compound bars into larger, amalgamated compound bars (Bars F and F).

Fig. 5. Development of 'complex' amalgamated compound bars, as seen in a selected simulation (Run 22) and in braided rivers. The left is the upstream for modelled rivers. (A) to (C) and (G) Maps of riverbed erosion and sedimentation for days 66, 74, 90 and 130. (D) Maps of near-bed sediment concentration for day 74. (F) Satellite image showing a complex compound bar. (G) Satellite images of a reach of the Songhua River, northern China, showing examples of compound bars of different style and size. The red frame shows the position of part (F).

Fig. 6. (A) Initial riverbed surface level with a gradient of 0.3 m/km. (B) Riverbed surface level at 2000 days, with a gradient of 0.29 m/km; this refers to the example shown in Fig. 3E. (C) Comparison between the riverbed surface at 0 and 2000 days; section location is shown in part (A). (D) Histogram showing the frequency distribution of changes in riverbed experienced by the 39 modelled rivers. (E) Box plot showing the

absolute values of changes in gradient, expressed relative to the initial gradient, for the 39 model runs.

Fig. 7. Bar morphology in modelled braided rivers with varying bed gradients and fixed discharge (1600 m^3/s). Abbreviations: BG = bed gradient; AWD = average water depth; Qw = flow discharge. (A) to (C) Maps of riverbed erosion and sedimentation produced by different runs, with bed gradients of 0.1 m/km, 0.5 m/km and 2.0 m/km, respectively. (D) Bar boundaries extracted from the part of map corresponding to Zone A in part (D).

Fig. 8. Satellite images of a reach of the Buha River, China, illustrating that bar aspect ratio tends to increase with increasing river slope. (A) Overview. (B) to (D) River reaches corresponding to Zone 1, Zone 2 and Zone 3 in part (A), respectively, and which have slopes of approximately 3.5 m/km, 1.9 m/km and 1.4 m/km, respectively.

Fig. 9. Bar morphology in braided rivers with the same bed gradient but variable discharge. (A) to (C) Maps of riverbed erosion and sedimentation for runs in which the river slope is 0.5 m/km, and the discharge values are 1370 m^3/s, 1960 m^3/s and 3080 m^3/s, respectively, corresponding to average water depths of 1.8 m, 2.2 m and 2.8 m, respectively. Abbreviations: BG = bed gradient; AWD = average water depth; Qw = flow discharge.

Fig. 10. Bar morphology in braided rivers with variable slope but the same average water depth across different runs. The left is the upstream for all the modelled rivers. The mean channel depths are similar, varying between 7.0 m to 7.2 m. (A) to (D) Maps of riverbed erosion and sedimentation for runs in which the gradient increases as follows: 0.3 m/km, 0.5 m/km, 1.0 m/km and 2.0 m/km. (E) to (H) Outlines of the braid bars identified in the corresponding maps (parts A to D). Abbreviation: BG = bed gradient.

Fig. 11. Statistics relating bar geometry to model characteristics and boundary conditions for 39 simulation runs. The total number of measured bars is 1400. R is the

Pearson's correlation coefficient; correlations are statistically significant at P = 0.01 (two-tailed). *Cv* denotes the coefficient of variation of bar areas for the same values of average water depth. (A) Box plots of bar areas. Model runs in each of groups 1 to 6 have the same initial bed gradient; runs in group 7 have the same water discharge. (B) Mean bar areas versus average water depth. Different runs in which the same average depth emerges show similar values of bar area, indicated by the small coefficients of variation. (C) Box plots of values of bar aspect ratio. (D) Mean values of bar aspect ratio versus river gradient. (E) Mean channel depth (river depth) versus average water depth (raster mean) for the 39 runs. (F) Bar mode versus bed gradient in different river width-to-depth ratios. (G) River depth versus mean bar area across 39 modelled rivers and 24 real-world rivers. The trend line between river depth and mean bar area proposed in this work is compared to that reported by Kelly (2006).

Fig. 12. (A) Mean bar mode versus river width-to-depth ratio across 44 real-world river reaches and the 39 modelled rivers. (B) Cross-plot of bar mode versus river width-to-depth ratio and riverbed gradient, across 44 real-world river reaches and the 39 modelled rivers. R^2 is the coefficient of determination; regressions are statistically significant at P = 0.01 (two-tailed). The underlying data are provided in Supplementary Tables A.1–A.3; see Supplementary Information.

Fig. 13. (A) Cross-plot of bar mode estimated using Eq. 5 versus observed bar mode for 44 real-world river reaches. (B) Cross-plot of riverbed gradient estimated using Eq. 7 versus observed riverbed gradient for 44 real-world river reaches; gradient estimations of two rivers (red ellipse) were excluded in the analyses as they are regarded as outliers. (C) Histogram displaying the discrepancy between estimated and observed values of bar mode. (D) Histogram displaying the discrepancy between estimated and

observed river gradient. The underlying data are provided in Supplementary Tables A.1 and A.2; see Supplementary Information.

Table 1. Settings and initial values for the main parameters of the Delft3D simulations. The morphological timescale factor determines the speed of morphological change (Deltares, 2014). A larger morphological timescale factor was set for simulations with slower development rates, and a lower morphological timescale factor for those with more rapid development.

Table 2. Settings of riverbed gradient, flow discharge and morphological timescale factors for the 39 Delft3D runs. The average (raster mean) water depth, sand concentration and the river depth for each run are also reported. The gradient is the same in each group and increases in Groups A to F. Runs 35 to 39 (Group G) are set up with the same discharge but different slopes. The imposed steady discharge can be seen as a bed-forming discharge, and is comparable to the bankfull discharge of natural rivers.

Table 3. Coefficients of variation (ratio of standard deviation to mean) of braid-bar areas and braid-bar width-to-depth ratios across the 39 modelled rivers. The underlying data are provided in Supplementary Data S.1 and S.2; see Supplementary Information.

List of Supplementary Items

Figure S1. (A) to (C) Time series of maps of riverbed erosion and sedimentation at 2000 days, 4000 days and 16000 days, respectively. (D) to (F) Sections of riverbed erosion and sedimentation at 2000 days, 4000 days and 16000 days, respectively, corresponding to parts (A) to (C), respectively. Section locations are also shown in parts (A) to (C), respectively. The simulation Run 10 is with an initial gradient of 0.3 m/km and discharge of 1780 m^3/s. No

significant unexpected channel incision observed at 4000 days, and only a limited degree of channel incision is shown at 16000 days, with unexpected channel incision <0.2 m.

Table A.1. Information on the geomorphology of 44 real-world braided rivers.

Table A.2. Data on bar area and channel depth across 24 real-world braided rivers.

Table A.3. Data on bar mode, river depth, river width-to-depth ratio and bed gradient across the 39 modelled braided rivers.

Supplementary Data S.1. Data on braid-bar area across the 39 modelled braided rivers.

Supplementary Data S.2. Data on length-to-width ratio across the 39 modelled braided rivers.

Table 1. Settings and initial values for the main parameters of the Delft3D simulations. The morphological timescale factor determines the speed of morphological change (Deltares, 2014). A larger morphological timescale factor was set for simulations with slower development rates, and a lower morphological timescale factor for those with more rapid development.

Parameter	Initial value / formula
Width of model domain	1000 m
Length of model domain	10000 m
Cell width (y)	5 m
Cell length (x)	10 m
Grain size range [a]	0.2 – 1 mm
Median grain size (D_{50})	0.6 mm
Formula of bed roughness	Manning
Turbulence model	K-Epsilon
Vertical grid points (layers)	5
Roughness formula	Manning
Dry density of sand	1650 kg/m^3
Dry density of mud	500 kg/m^3
Threshold depth	0.1 m
Threshold sediment thickness	0.05 m
Perturbation: maximum initial bed level	0.01 m
Vertical eddy viscosity	0.2 m^2/s
Vertical eddy diffusivity	0.1 m^2/s
Hydrodynamic time step	6 s
Factor for erosion of adjacent dry cells	0.5
Time span of the braided model	2 years
Initial transverse riverbed gradient	Zero
Vegetation	None
Morphological timescale factor [b]	96, 48 or 24

[a] The grain size follows a log-normal distribution.
[b] Values of all runs are provided in Table 2.

Table 2. Settings of riverbed gradient, flow discharge and morphological timescale factors for the 39 Delft3D runs. The average (raster mean) water depth, sand concentration and the river depth for each run are also reported. The gradient is the same in each group and increases in Groups A to F. Runs 35 to 39 (Group G) are set up with the same discharge but different slopes.

Grope No.	Run No.	Riverbed gradient (m/km)	Discharge (m^3/s)	Sand concentration (kg/m^3)	Average water depth (m)	River depth (m)	Morphological timescale factor
A	1	0.1	613	0.0018	1.8	5.76	96
	2	0.1	744	0.0032	2.0	6.40	96
	3	0.1	880	0.0040	2.2	7.04	96
	4	0.1	1030	0.0048	2.4	7.68	96
	5	0.1	1365	0.0061	2.8	8.97	96
B	6	0.3	860	0.014	1.6	5.02	96
	7	0.3	1060	0.017	1.8	5.79	96
	8	0.3	1300	0.021	2.0	6.47	96
	9	0.3	1520	0.027	2.2	7.13	96
	10	0.3	1780	0.032	2.4	7.71	96
	11	0.3	2395	0.040	2.8	9.15	96
C	12	0.5	1110	0.030	1.6	4.93	48
	13	0.5	1370	0.037	1.8	5.71	48
	14	0.5	1640	0.048	2.0	6.26	48
	15	0.5	1960	0.062	2.2	7.22	48
	16	0.5	2300	0.079	2.4	7.79	48
	17	0.5	3080	0.111	2.8	9.05	48
D	18	1.0	1570	0.127	1.6	5.02	24
	19	1.0	1920	0.152	1.8	5.89	24
	20	1.0	2350	0.173	2.0	6.24	24
	21	1.0	2765	0.193	2.2	7.22	24
	22	1.0	3250	0.210	2.4	7.53	24
	23	1.0	4260	0.236	2.8	8.81	24
E	24	2.0	1932	0.304	1.6	5.01	24
	25	2.0	2465	0.361	1.8	5.77	24
	26	2.0	3160	0.426	2.0	6.60	24
	27	2.0	4055	0.495	2.2	7.05	24
	28	2.0	5320	0.590	2.4	7.85	24
	29	2.0	7780	0.768	2.8	9.15	24
F	30	4.0	2560	0.862	1.6	5.24	24
	31	4.0	3320	0.955	1.8	5.93	24
	32	4.0	4385	1.040	2.0	6.26	24
	33	4.0	5850	1.163	2.2	7.08	24
	34	4.0	8090	1.271	2.4	7.79	24
G	35	0.1	1600	0.007	3.0	9.79	96
	36	0.3	1600	0.0297	2.27	7.09	96
	37	0.5	1600	0.0451	1.95	6.06	48
	38	1.0	1600	0.1276	1.62	5.06	24
	39	2.0	1600	0.2618	1.35	4.43	24

Table 3. Coefficients of variation of bar areas and bar width-to-depth ratios across the 39 modelled rivers. The underlying data are provided in Data S.1 and S.2; see Supplementary Information.

Run No.	CV of bar areas	CV of bar length/width ratio
1	0.26	0.23
2	0.28	0.24
3	0.25	0.23
4	0.27	0.25
5	0.27	0.26
6	0.26	0.26
7	0.27	0.25
8	0.29	0.27
9	0.27	0.20
10	0.28	0.26
11	0.29	0.18
12	0.27	0.21
13	0.28	0.21
14	0.27	0.23
15	0.28	0.25
16	0.23	0.27
17	0.26	0.21
18	0.28	0.21
19	0.28	0.19
20	0.28	0.25
21	0.28	0.24
22	0.29	0.21
23	0.26	0.16
24	0.28	0.20
25	0.27	0.22
26	0.28	0.22
27	0.29	0.20
28	0.28	0.20
29	0.26	0.22
30	0.21	0.18
31	0.28	0.18
32	0.29	0.19
33	0.28	0.18
34	0.29	0.21
35	0.24	0.17
36	0.24	0.21
37	0.22	0.21
38	0.26	0.24
39	0.20	0.20

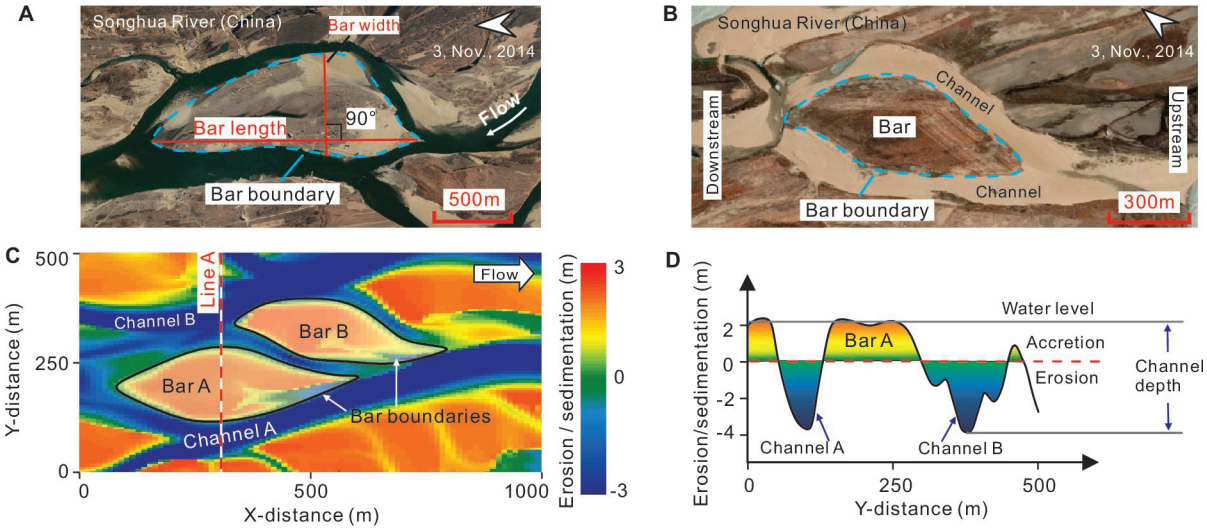

sed_13040_figure 1.eps

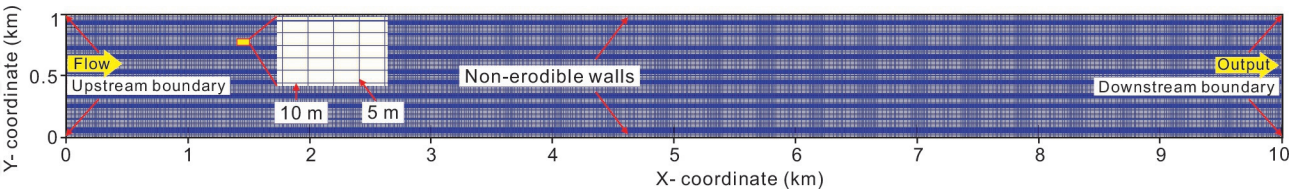

sed_13040_figure 2.eps

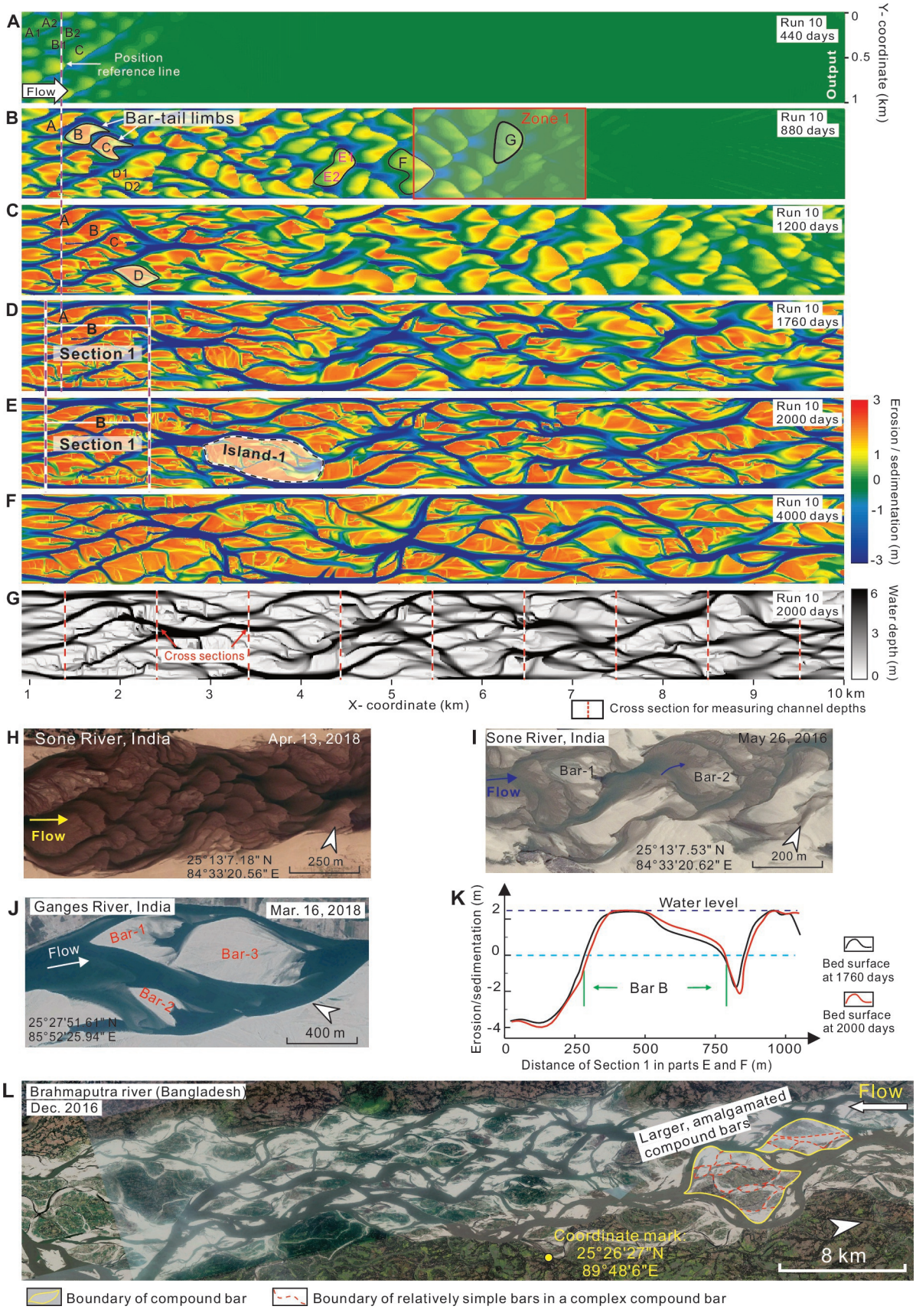

sed_13040_figure 3.eps

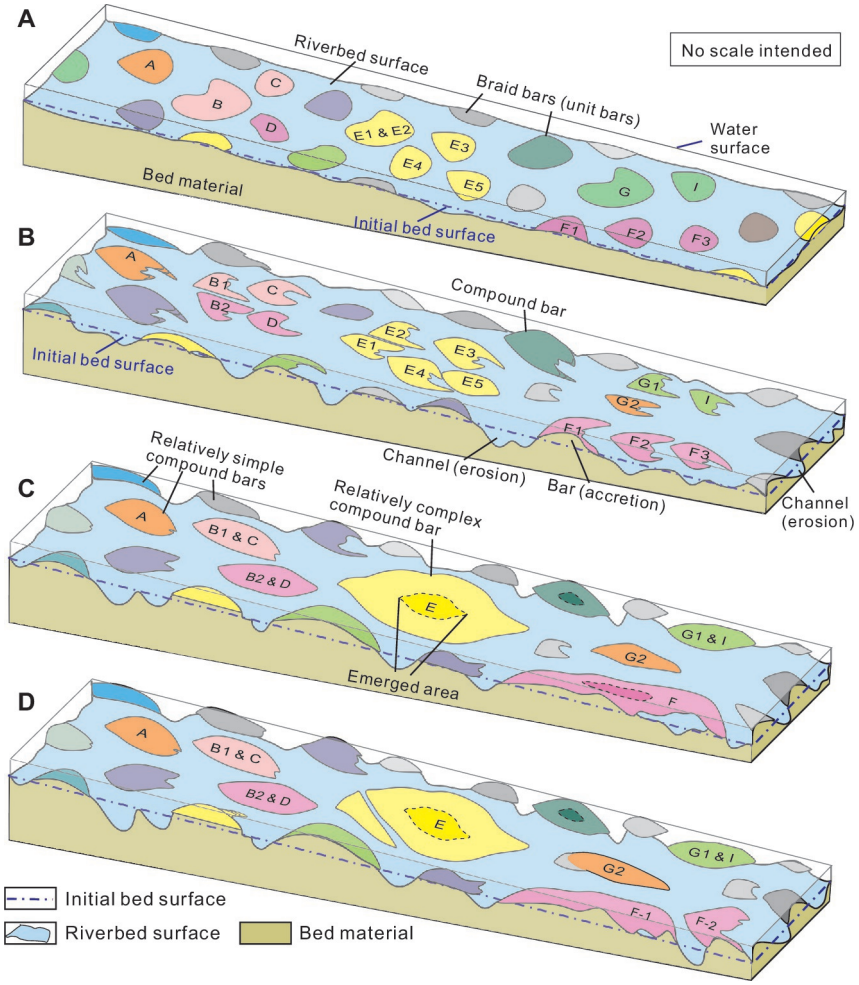

sed_13040_figure 4.eps

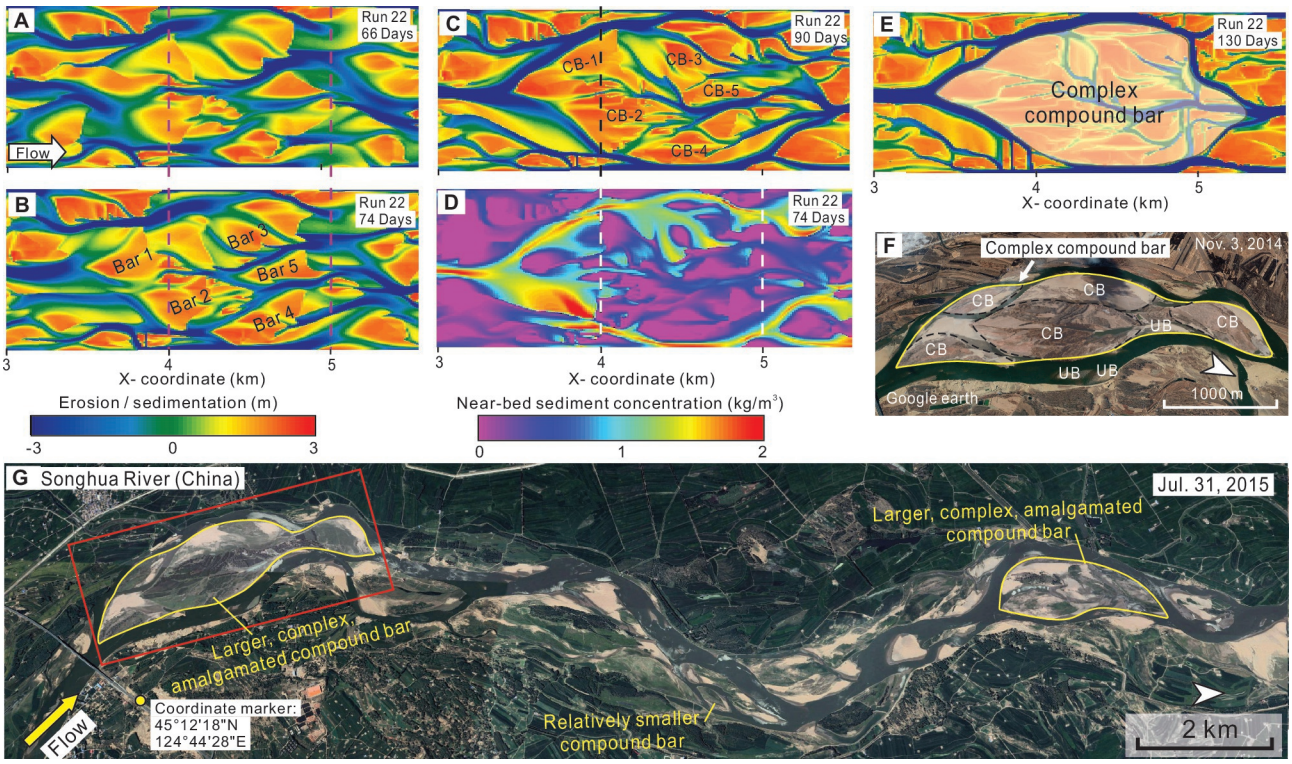

sed_13040_figure 5.eps

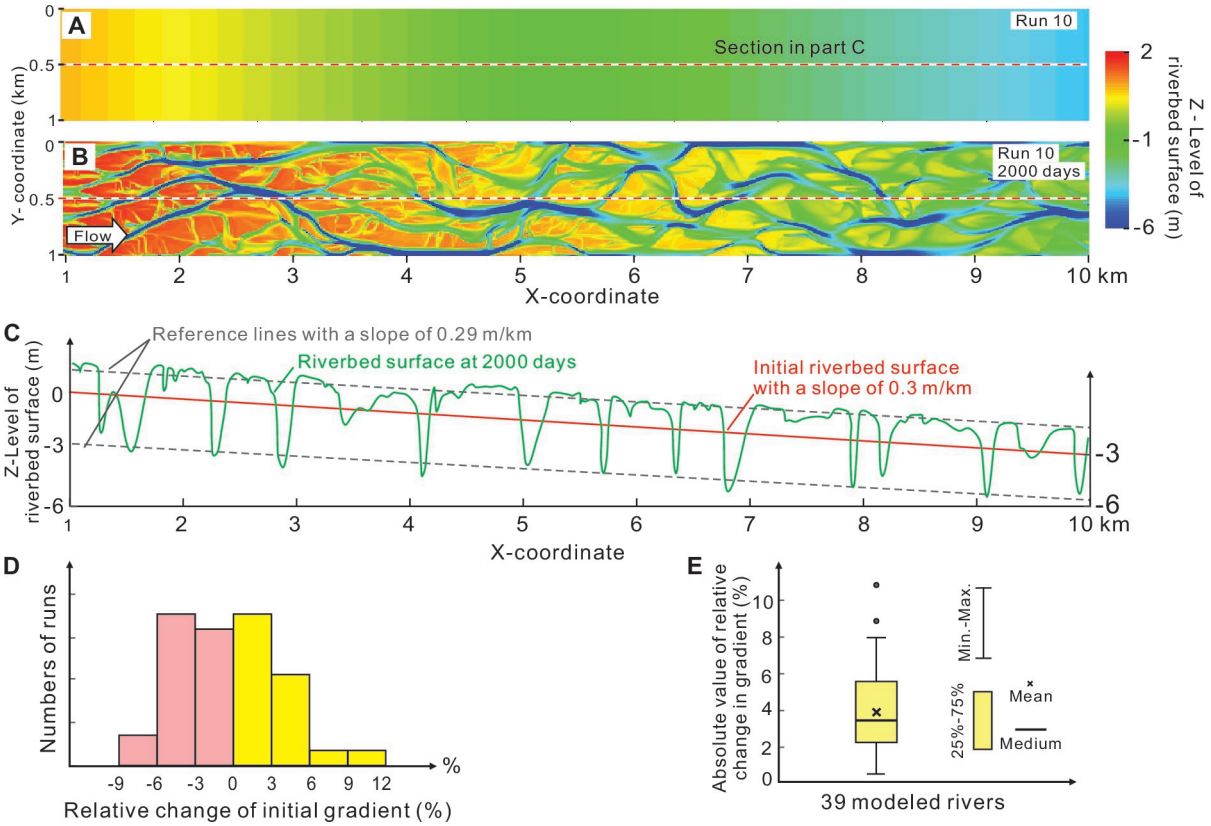

sed_13040_figure 6.eps

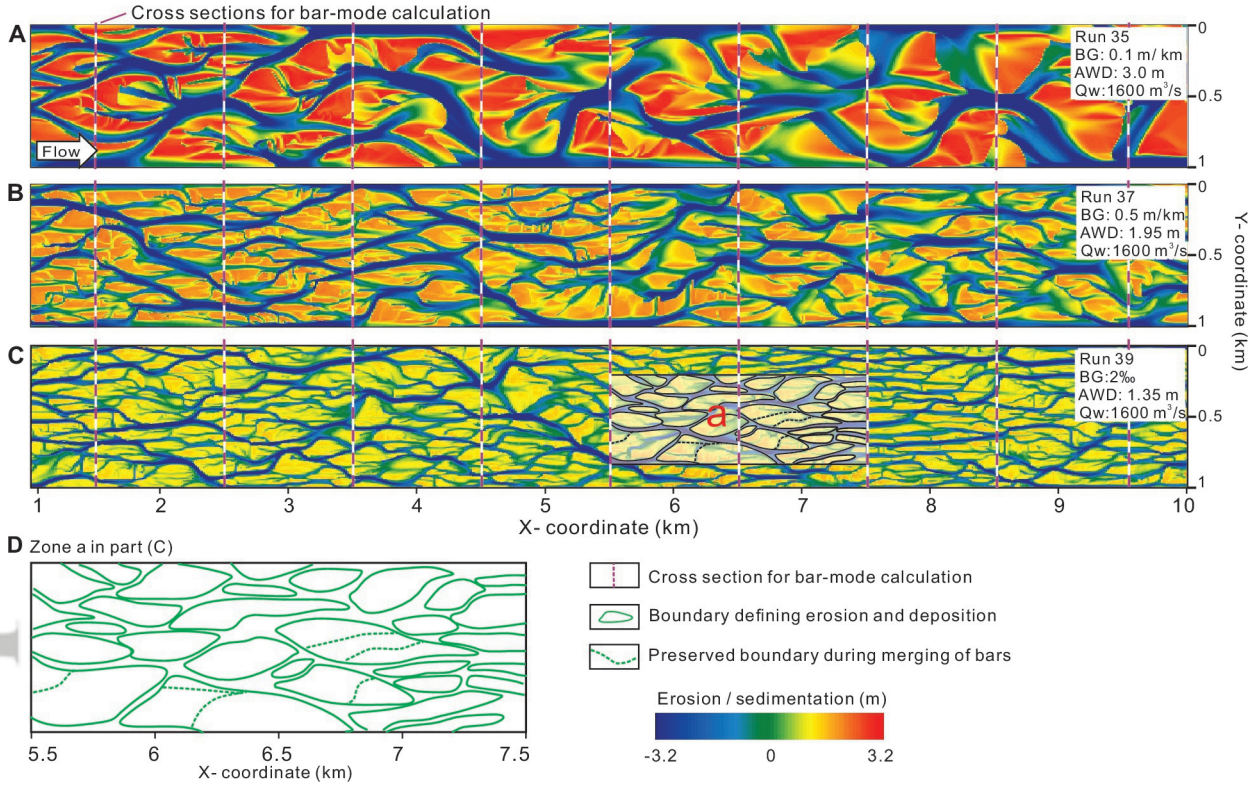

sed_13040_figure 7.eps

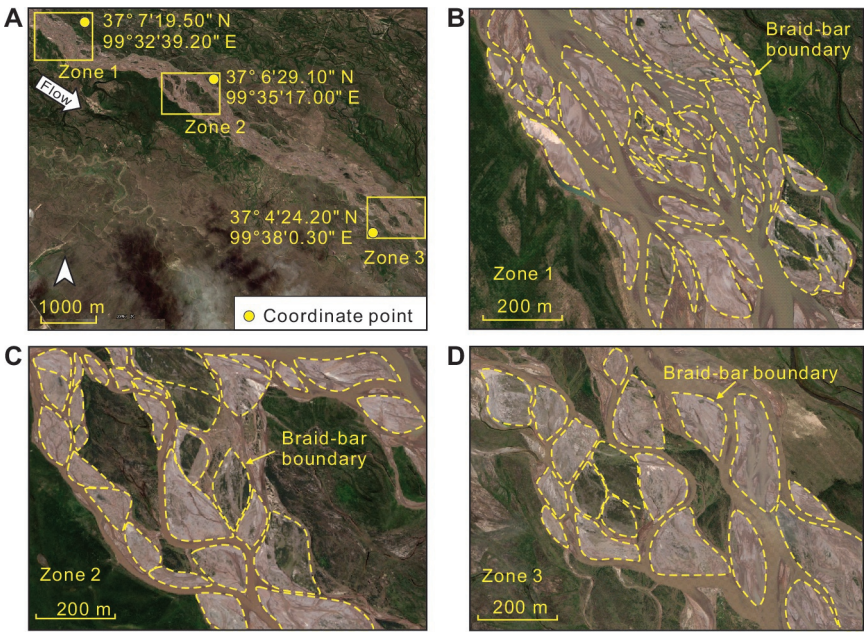

sed_13040_figure 8.eps

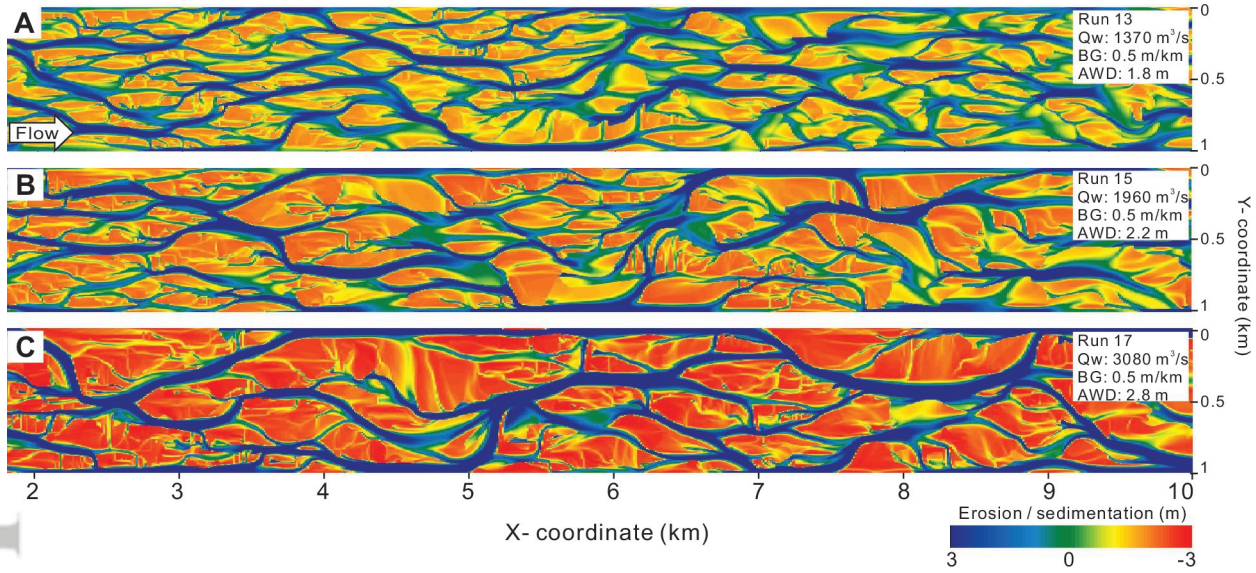

sed_13040_figure 9.eps

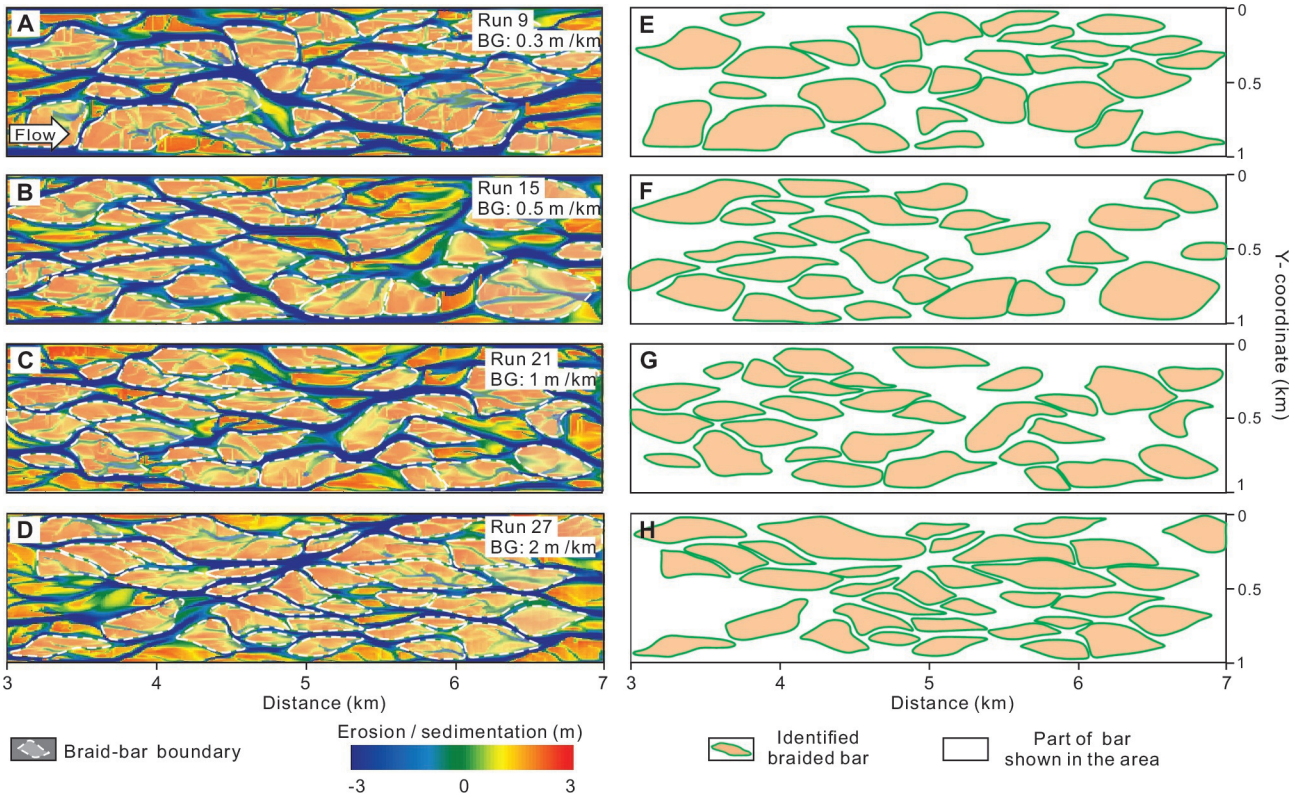

sed_13040_figure 10.eps

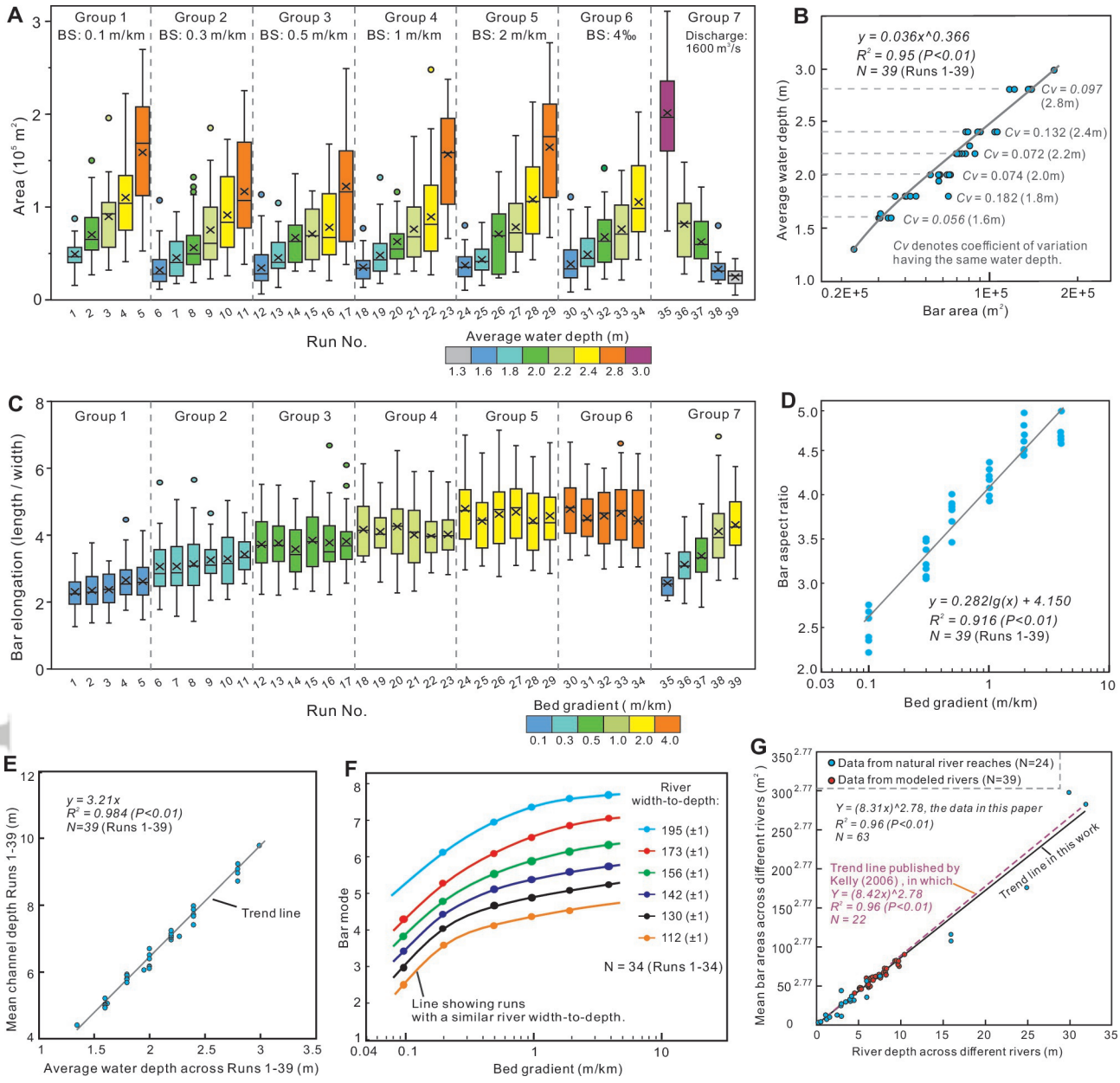

sed_13040_figure 11.eps

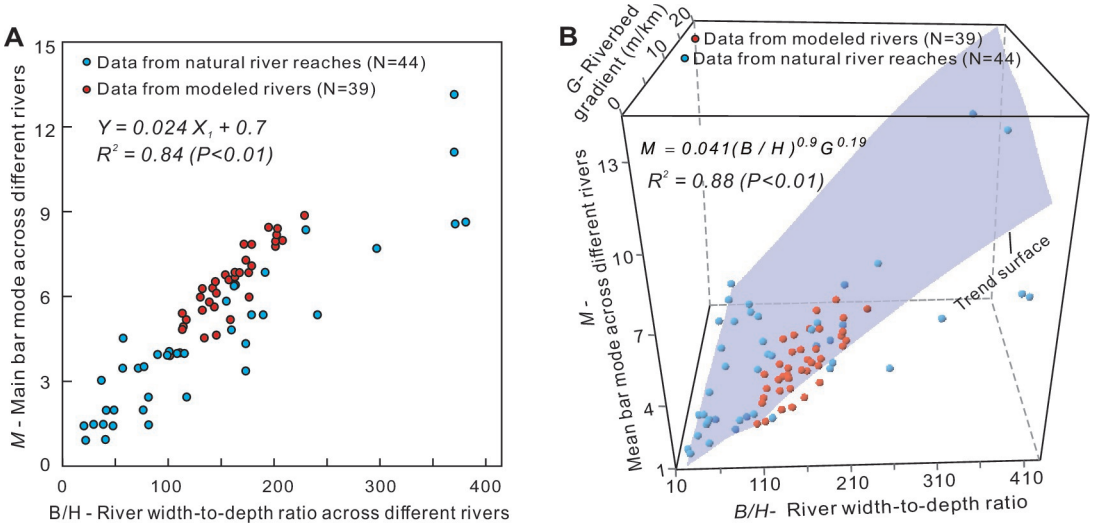

sed_13040_figure 12.eps

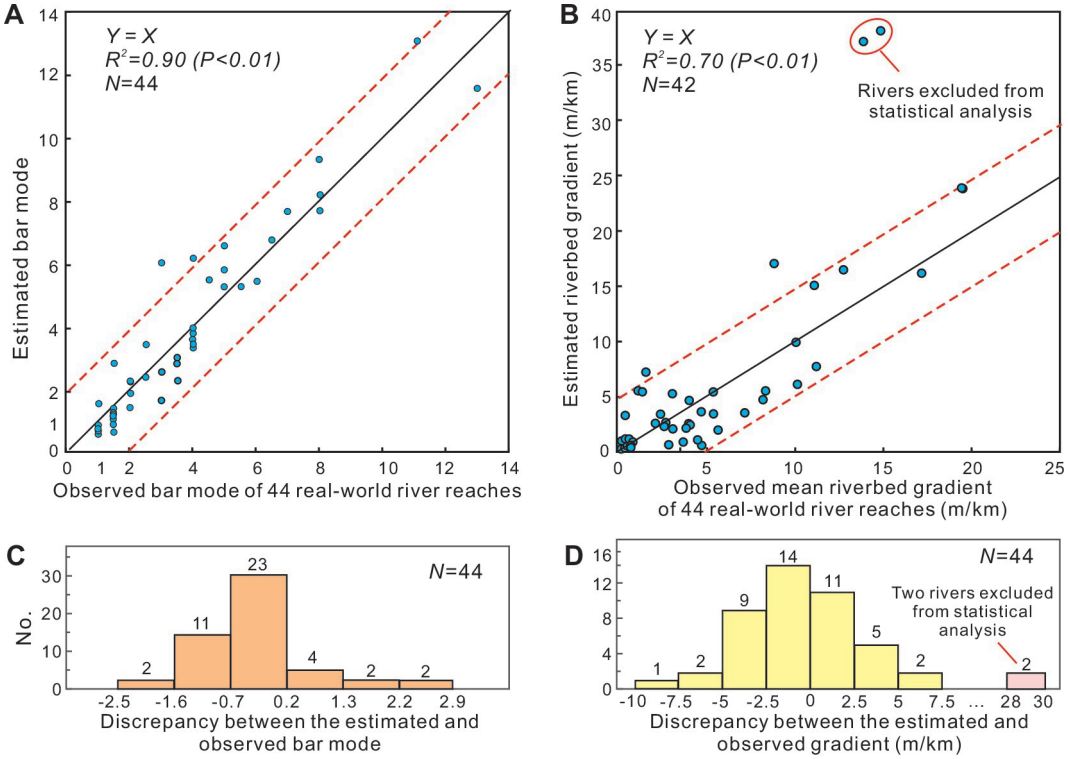

sed_13040_figure 13.eps